Pressure-dependent fouling behavior during sterile filtration of mRNA-containing lipid nanoparticles

Kevork Oliver Messerian[a], Anton Zverev[b], Jack F. Kramarczyk[b] and Andrew L. Zydney[a]*

[a]Department of Chemical Engineering
The Pennsylvania State University
University Park, PA 16802

[b]Moderna, Inc.
Cambridge, MA 02139

Beste Grüße, Dan :-)

Communication concerning this manuscript should be addressed to:
Andrew Zydney, Department of Chemical Engineering,
The Pennsylvania State University, University Park, PA 16802
Phone: 814-863-7113, Fax: 814-865-7846
E-mail: zydney@engr.psu.edu

Abstract

The COVID-19 pandemic has generated growing interest in the development of mRNA-based vaccines and therapeutics. However, the size and properties of the lipid nanoparticles (LNPs) used to deliver the nucleic acids can lead to unique phenomena during manufacturing that are not typical of other biologics. The objective of this study was to develop a more fundamental understanding of the factors controlling the performance of sterile filtration of mRNA-LNPs. Experimental filtration studies were performed with a Moderna mRNA-LNP solution using a commercially available dual-layer polyethersulfone sterile filter, the Sartopore 2 XLG. Unexpectedly, increasing the transmembrane pressure (TMP) from 2 to 20 psi provided more than a two-fold increase in filter capacity. Also surprisingly, the effective resistance of the fouled filter decreased with increasing TMP, in contrast to the pressure-independent behavior expected for an incompressible media and the increase in resistance typically seen for a compressible fouling deposit. The mRNA-LNPs appear to foul the dual-layer filter by blocking the pores in the downstream sterilizing-grade membrane layer, as demonstrated both by scanning electron microscopy (SEM) and derivative analysis of filtration data collected for the two layers independently. These results provide important insights into the mechanisms governing the filtration of mRNA-LNP vaccines and therapeutics.

Introduction

The COVID-19 pandemic has highlighted the enormous potential of mRNA-based vaccines, with the first two vaccines approved for protection against COVID-19 infection employing mRNA that encodes the SARS-Cov-2 spike protein.[1-5] mRNA therapeutics are of growing interest because of their high efficacy, rapid development timelines, and excellent safety profiles.[6-10] In addition to vaccines against infectious diseases, mRNA can be used to treat auto-immune disorders, cardiovascular diseases, a wide range of cancers, and injured or diseased tissues.[6,11-13]

One of the key challenges in mRNA-based therapeutics is insuring effective delivery of the mRNA to the targeted cells.[14-17] Although several non-viral delivery systems have been developed, including polymer-based carriers and inorganic nanoparticles, the greatest success has been achieved with lipid nanoparticles (LNPs).[6-8,10,13,18,19] LNPs are complex multicomponent systems typically composed of four distinct lipid species: ionizable cationic lipids that neutralize the negatively charged mRNA and facilitate intracellular uptake, cholesterol that stabilizes the LNP and facilitates transfection, phospholipids that support the general structure of the LNP and promote endosomal escape,[2-5,9-16] and polyethylene glycol-anchored lipids that reduce non-specific binding and increase circulation half-life.[20-22] The resulting mRNA-LNPs are typically 50-200 nm in diameter[23-25] and can vary from highly spherical to more ellipsoidal geometries.[14,16,18]

The production of mRNA vaccines begins with the *in vitro* enzymatic synthesis of the mRNA from a DNA template.[6,7,23,26] The downstream purification process involves a series of chromatographic separations and tangential flow filtration.[27-29] The purified mRNA is encapsulated in the LNP by mixing the mRNA (in an acidic aqueous buffer) with the lipids (in ethanol).[2,8,17] The resulting LNP suspension is buffer exchanged and concentrated by ultrafiltration / diafiltration followed by sterile filtration[27] as part of the final fill-finish operation.[30-32]

Sterile filtration is a critical manufacturing step that ensures pharmaceutical products are essentially free of microbial contaminants.[33] Sterile filtration is commonly performed using normal-flow (dead-end) filtration through membranes containing 0.2 μm-rated pores, which can completely retain a microbial challenge of 10^7 colony forming units / cm^2 of filter area.[34,35] The sterile filtration unit operation can be characterized by investigating the filter capacity (batch size), transmission (product yield), and product quality. Sterile filtration of LNPs, as well as other large

viral and non-viral delivery vehicles, can be challenging because these products can be similar in size to the 0.2 μm pore size rating of sterilizing-grade filters.[36] For example, Taylor et al. examined the sterile filtration of a live attenuated viral vaccine with mean particle size ranging from 100-400 nm through a range of sterile filters, including both single- and dual-layer filters, with the vaccine transmission ranging from less than 2% to more than 80%.[37] Emami et al. reported high yield (>95%) but more than a 7-fold difference in capacity during sterile filtration of different glycoconjugate serotypes even though these glycoconjugate vaccines differed by less than a factor of two in their measured particle size.[38] Zourna et al. evaluated the sterile filtration of liposomes using a polyethersulfone filter, with a 40-fold increase in capacity achieved by reducing the size of the liposomes from 179 to 127 nm and an 18-fold increase in capacity attained by increasing the differential pressure from 0.7 to 4.1 bar.[39] The authors hypothesized that the increase in capacity with increasing pressure was due to either a change in liposome size and shape or reduced interactions with the membrane pores associated with the shorter residence time, although no detailed analysis of these phenomena was provided. Although several studies have described the sterile filtration of liposomes,[39-43] there do not appear to be any published data on the sterile filtration of mRNA-LNPs or any other lipid nanoparticles.

The objective of this study was to develop a more fundamental understanding of the factors controlling the performance of sterile filtration of mRNA-LNPs ("LNPs") using the dual-layer (0.8 μm / 0.2 μm) Sartopore 2 XLG sterilizing grade filter. Data were obtained over a range of transmembrane pressures (TMP), with the fouled membranes examined by scanning electron microscopy to obtain additional insights into the fouling behavior. The results provide important insights into the underlying mechanisms affecting the filtration behavior of mRNA-LNPs.

Methods

Materials

Experiments were performed with an mRNA-LNP solution (LNP) provided by Moderna Inc. (Cambridge, MA). The frozen LNP solution was thawed in a room temperature water bath before use.

Sterile filtration data were obtained using Sartopore 2 XLG dual-layer asymmetric polyethersulfone (PES) filters consisting of a 0.8 μm-rated pore size layer on top of a 0.2 μm-rated (sterilizing grade) layer. Unless otherwise specified, the membranes were sealed in 25-mm

diameter capsules provided by the manufacturer (Sartorius). Limited data were obtained with the individual layers of the filter housed at the base of a 25-mm Amicon 8010 filtration cell (MilliporeSigma, Bedford, MA) operated without the magnetic stirrer, with a 5 μm pore size nylon mesh placed beneath the filter membrane to promote flow distribution.

Filtration Experiments

Filtration experiments were performed at constant transmembrane pressure. The filter capsule was fed by a 1-liter stainless-steel feed reservoir (Alloy Products Corporation, WI) pressurized with compressed air and controlled using a pressure regulator. The TMP was monitored using an Ashcroft digital pressure gauge placed immediately upstream of the filter, with the permeate outlet maintained at atmospheric pressure. The membranes were initially flushed with a minimum of 100 L/m^2 of deionized water followed by a Tris-sucrose formulation buffer, with the latter prepared by mixing appropriate quantities of Tris-base (MilliporeSigma, Catalog Number 9210), Tris–HCl (Invitrogen, 15567-027) and sucrose (MilliporeSigma, 8550) to obtain a 20 mM Tris concentration and 87 g/L sucrose at pH 7.5. The membrane hydraulic permeability was evaluated by measuring the filtrate flux at several TMP (up to 70 kPa) using the Tris-sucrose buffer. All experiments were performed at room temperature (21 ± 1 ºC).

The feed reservoir and filter capsule were then emptied, refilled with the LNP solution, and the system re-pressurized. Filtrate flow was evaluated by continuous mass readings on an OHAUS Ranger™ 3000 scale, with the data logged every second using the OHAUS Serial Port Data Collection Software. Permeate concentrations were evaluated based on UV absorbance at 230 nm using a Tecan microplate reader (Mannedorf, Switzerland).

LNP / Filter Characterization

The LNP size distribution was determined by Dynamic Light Scattering (DLS) using a Malvern Zetasizer Nano ZS90 (Malvern, United Kingdom). Samples were analyzed at 20ºC after equilibration for 120 s. The light scattering intensity was evaluated for a total of 10 runs. All experiments were performed with LNPs whose properties were consistent with those described by Hassett et al.[44] and Brader et al.[16] The mean LNP diameter was between 100 and 150 nm and the LNP concentration was on the order of ~10^{12} particles per mL.

LNPs captured on the external surface of the filter were examined by scanning electron microscopy (SEM). The fouled membrane was removed from the filtration cell, dried inside a

Fisher Isotemp® 200 Series oven at 30 ºC for one hour, and cut into small pieces before being mounted on conductive pins with a double-sided carbon tape. A thin layer of gold/platinum was applied using a Bal-tec SCD 050 Sputter coater. Surface images were obtained with a Zeiss SIGMA VP-FESEM at 3.0 kV.
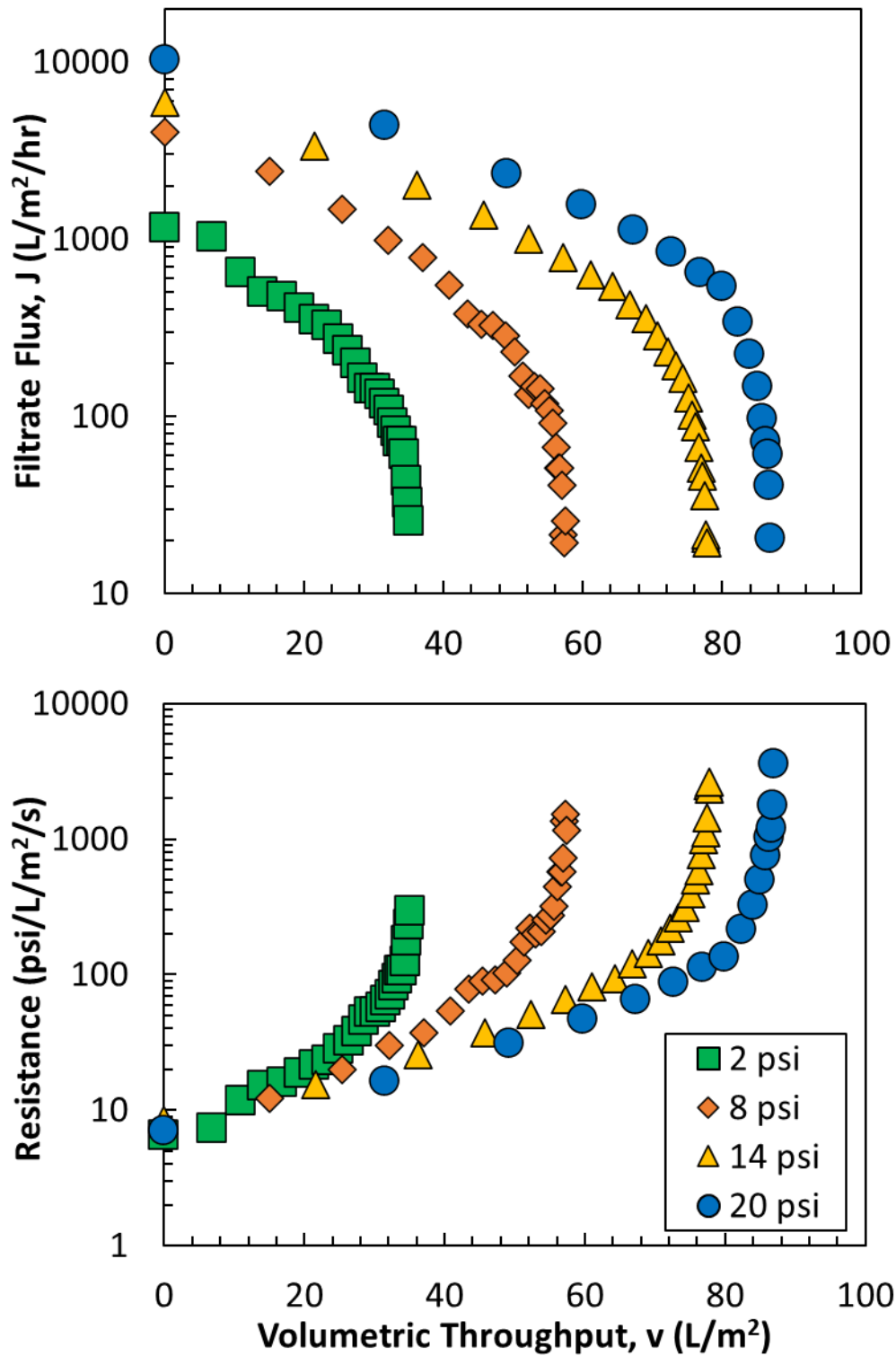
Results & Discussion

Sterile Filtration Performance

Figure 1 displays the filtrate flux profiles during constant pressure filtration of the LNPs through the Sartopore 2 XLG capsules at pressures of 2, 8, 14, and 20 psi (14, 55, 97, and 140 kPa). The overall LNP yield was greater than 96% in all experiments, with no apparent loss of transmission even at very high degrees of fouling. Dynamic light scattering (DLS) analysis of the permeate and feed samples showed no substantial change in the LNP size distribution, with the Z-average diameter for the permeate samples within 2% of that for the feed. The initial filtrate flux (J_o) was approximately equal to the buffer flux evaluated immediately prior to the filtration experiment (at the same TMP), with the J_o values increasing linearly with increasing TMP, consistent with a constant membrane permeability. The filtrate flux (J) is plotted as a function of the volumetric throughput (v), defined as the ratio of the cumulative filtrate volume (V) to the membrane area (A). In each case, the curves are concave down on the semi-log plot, with the absolute value of the slope increasing with increasing throughput. The initial rate of flux decline, -dJ/dv, decreases with increasing transmembrane pressure, while the filter capacity (V_{max}), evaluated as the volumetric throughput at which the filtrate flux declines to 10% of its initial value, increases from 32 L/m^2 at 2 psi to 69 L/m^2 at 20 psi. For most biologics, increasing transmembrane pressure during sterile filtration results in either decreased capacity or constant capacity.[45] The observed large increase in capacity for filtration of LNPs, and decrease in rate of flux decline, is unusual for most sterile filtration processes, although it is consistent with the increase in capacity with increasing TMP reported by Zourna et al.[39] for the sterile filtration of Lipoid S100 liposomes.

The filtrate flux data are replotted in the lower panel of Figure 1 as the total resistance, R:

$$R = \frac{TMP}{J} \qquad (1)$$

where TMP is the transmembrane pressure and J is the filtrate flux, both evaluated at the same volumetric throughput. The resistance data tend to follow single curve near the start of the filtration; this is consistent with a constant (pressure-independent) permeability during the initial phase of the filtration. However, the resistance curves at higher pressures increase more slowly than the resistance curves at lower pressures, leading to an increase in filter capacity with increasing TMP.

Figure 1: Filtrate flux (upper panel) and resistance (lower panel) as a function of the volumetric throughput during constant pressure filtration of the LNP through the Sartopore 2 XLG capsules at pressures of 2, 8, 14 and 20 psi.

Fouling Mechanism

Additional insights into the underlying fouling behavior were obtained by replotting the flux data in the form suggested by Hermans and Bredee:[46]

$$\frac{d^2t}{dv^2} = k \left(\frac{dt}{dv}\right)^n \tag{2}$$

where t is the filtration time, v is the throughput (filtrate volume per unit membrane area), and k is a proportionality constant with units dependent on the value of n. All four of the classical blocking models can be described by Equation (2) with the power-law exponent defining the fouling mechanism: $n = 2$ corresponds to complete pore blockage (in which foulants block pore entrances), $n = 3/2$ corresponds to pore constriction (in which the pore radius decreases as foulants deposit along the pore walls), $n = 1$ corresponds to intermediate pore blockage (in which foulants either block pore entrances or deposit on previously blocked pores), and $n = 0$ corresponds to cake filtration (in which foulants accumulate on the membrane surface in a permeable cake).[47-51] Results are shown in Figure 2 with all derivatives evaluated numerically using a finite difference analysis accounting for the non-constant intervals for the volumetric throughput (accurate to second order in Δv), with the derivative averaged over approximately 20s intervals to minimize numerical noise. The data for the LNPs all show a slope of $n \approx 2$ on the log-log plot over the entire filtration experiment, consistent with predictions of the complete pore blockage model.
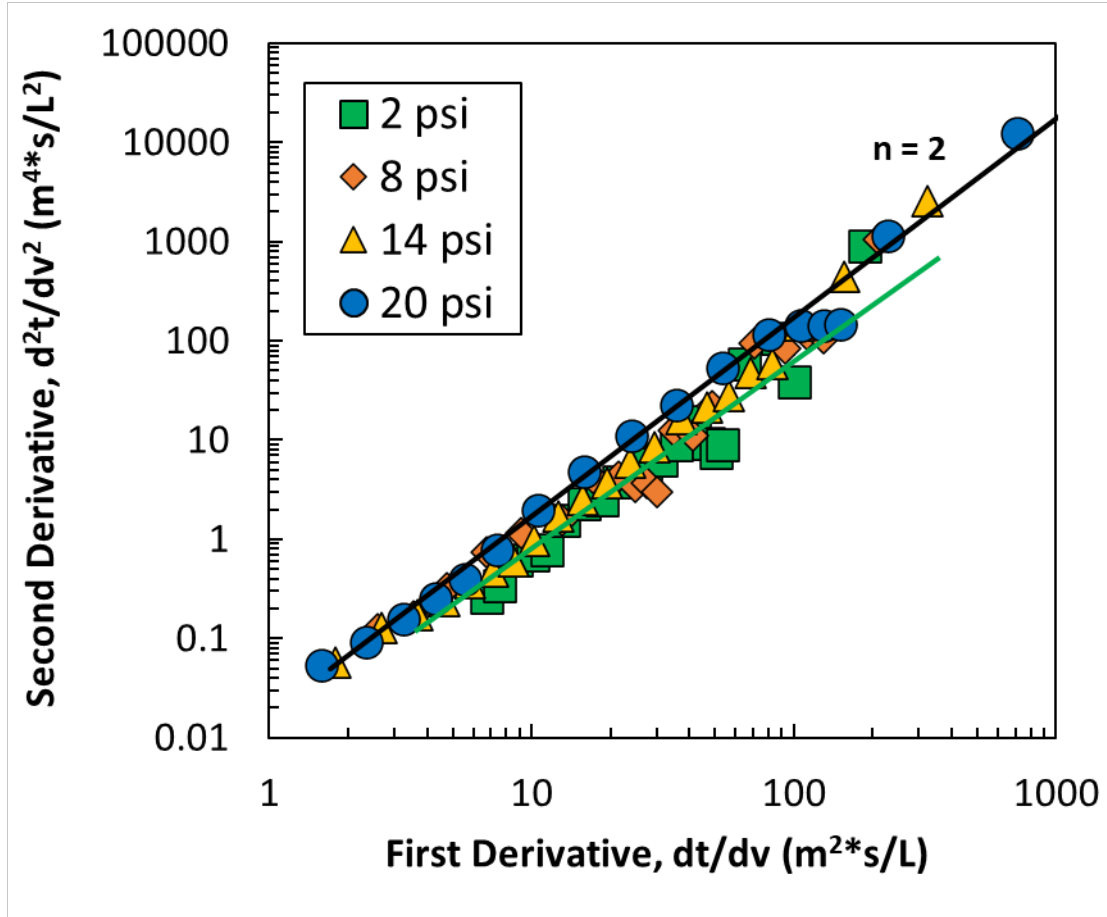
Figure 2: Derivative plot for LNP filtration at 2, 8, 14 and 20 psi through the Sartopore 2 XLG. The solid black and green lines represent a slope of 2 to guide the eye; these are not fits to the experimental data.

To further investigate the origin of the underlying fouling mechanisms, filtration experiments were performed using the individual layers of the Sartopore 2 XLG, along with the dual-layer membrane, all housed in an ultrafiltration cell. Figure 3 shows the flux profiles as a function of volumetric throughput at a constant pressure of 14 psi (100 kPa); the lower capacity of the dual-layer filter compared to that seen in Figure 1 reflects batch-to-batch variability in the results (all of the data in any single figure were obtained with the same batch of LNPs). Both the 0.2 and 0.8 μm layers showed high LNP transmission (>96%), with no measurable change in LNP size in the filtrate samples as determined by DLS. The 0.8 μm layer alone had the highest filtrate flux and lowest rate of flux decline, with a capacity of V_{max} = 230 L/m^2 (again defined as the throughput corresponding to 90% flux decline). The 0.2 μm layer alone showed a rapid flux decline and small capacity of V_{max} = 16 L/m^2. The dual-layer filter showed an intermediate capacity of

V_{max} = 39 L/m², substantially smaller than the 0.8 µm layer alone yet almost two and a half-fold higher than the 0.2 µm layer. These results demonstrate that the bulk of the fouling occurs in the sterilizing-grade 0.2 µm layer of the Sartopore 2 XLG, with the 0.8 µm prefilter providing protection to the downstream layer, likely by retaining foulants that are present in the feed.
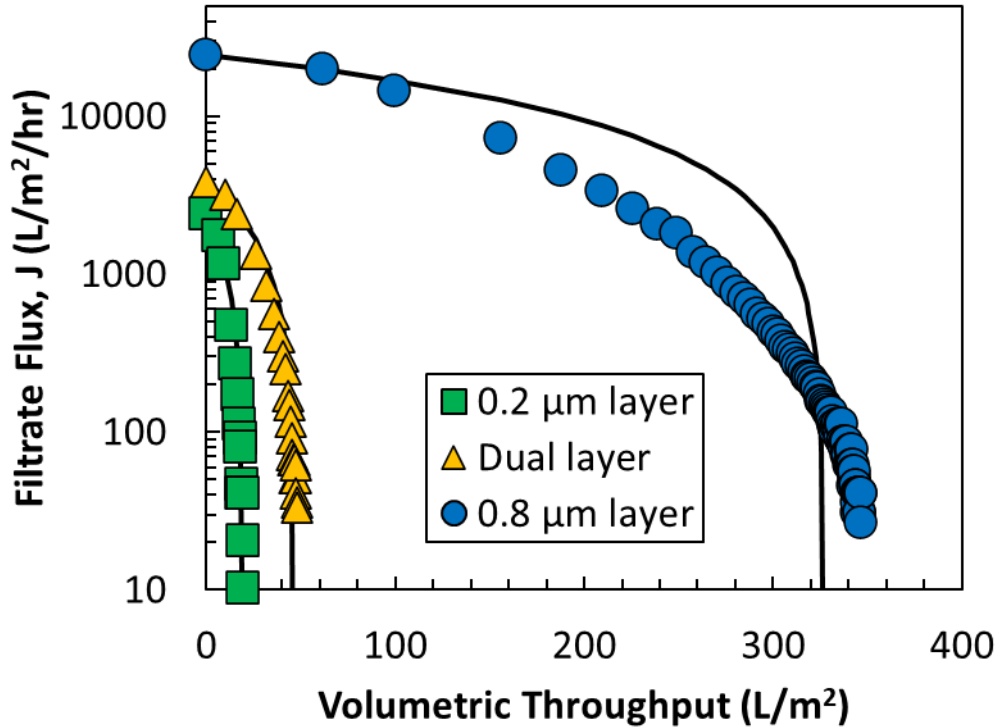
Figure 3: Filtrate flux as a function of the volumetric throughput for filtration through the individual layers of the Sartopore 2 XLG at TMP = 14 psi. Solid curves are model fits generated using the linearized form of the complete pore blockage model.

The solid curves in Figure 3 were obtained using the classical form of the complete pore blockage model:[51]

$$J = J_0 (1 - \alpha v) \qquad (3)$$

with the best-fit value of α, a parameter describing the rate of blockage with units of m²/L, determined by non-linear regression using Mathematica. The model closely fits the flux data for both the 0.2 µm layer alone and for the dual layer (α = 0.053 and 0.022 m²/L, respectively, with R^2 values > 0.98), providing further support for the assertion that LNP fouling is predominantly

due to pore blockage in the 0.2 μm layer; the smaller value of α for the dual layer filter reflects the removal of foulants by the prefilter. In contrast, the complete pore blockage model poorly fits the flux data for the 0.8 μm layer alone, suggesting that the fouling observed in this layer is not completely described by a pore blockage mechanism. The substantial difference in capacity between the individual membrane layers, as well as the difference in fouling mechanisms, suggests that the major foulants are likely smaller than 0.8 μm in size. This points to LNPs themselves as the primary foulants rather than higher order, large-scale aggregates.

Further insights into the fouling behavior were obtained by collecting and pooling the permeate from three separate filtration runs and using that as the feed for a second filtration through a fresh Sartopore 2 XLG membrane. All filtration experiments were performed on the same day, with the collected permeate used within 1 hour of the first filtration. Results for this "re-filtered" LNP are shown in Figure 4 along with data for one of the original filtration runs, all performed at 14 psi. The re-filtered LNP shows a much slower rate of fouling, with a filter capacity approximately 2-fold larger than that of the fresh feed. The higher capacity for the re-filtered LNP indicates that, despite the very high overall transmission, a portion of foulants was removed during the first filtration. In addition, although foulants were removed during the first filtration, they were not removed completely: the general fouling behavior during re-filtration was unchanged, with pore blockage still the dominant mechanism. This suggests that fouling might occur by a stochastic mechanism, with a small fraction of the LNPs being captured by the sterilizing-grade layer of the Sartopore 2 XLG membrane. This fouling behavior may depend on the individual particle morphology and surface characteristics, flow velocity, and/or membrane pore structure at specific locations on the filter.
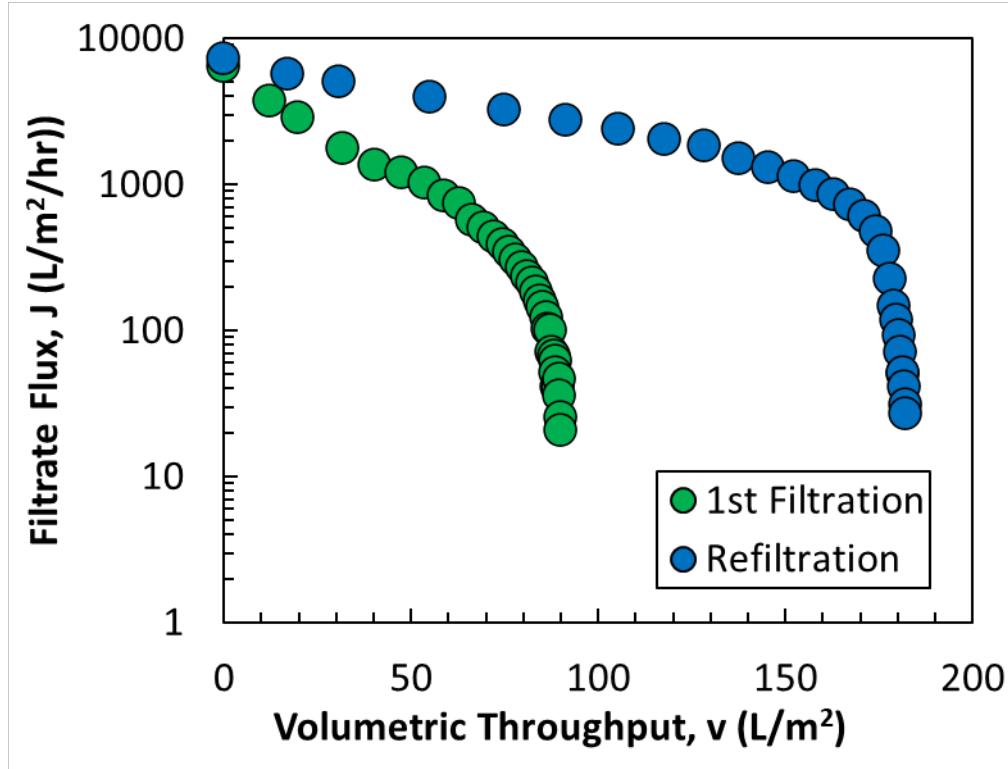
Figure 4: Filtrate flux as a function of volumetric throughput during filtration of the fresh LNP and previously filtered LNP through the Sartopore 2 XLG at 14 psi.

### *Characterization of fouled filter*

The nature of the LNP fouling was examined by SEM as shown in Figure 5. Images were obtained of the surfaces of the individual layers of the Sartopore 2 XLG after filtration of buffer (i.e., no fouling) and filtration of LNPs through the dual-layer filter at 14 psi until a flux decline of more than 99%. The 0.8 µm layer appears to have a rough, asymmetric surface with relatively low pore density, while the 0.2 µm layer is substantially smoother with a higher density of relatively circular pore openings. There is no visible difference in the 0.8 µm prefilter after fouling, suggesting most of the pores remain fully open, which is consistent with the very high filtration capacity when the 0.8 µm layer was used alone (Figure 3). In contrast, much of the surface of the 0.2 µm layer is covered with LNPs, appearing as an aggregated layer on top of the membrane. It is important to note that the structure and organization of the LNPs seen in the SEM image may be affected by the sample preparation (drying) and appear different in the native (wetted)

environment, although the high degree of surface fouling is fully consistent with the pore blockage mechanism identified by the derivative analysis in Figure 2.

Clean 0.8 μm layer
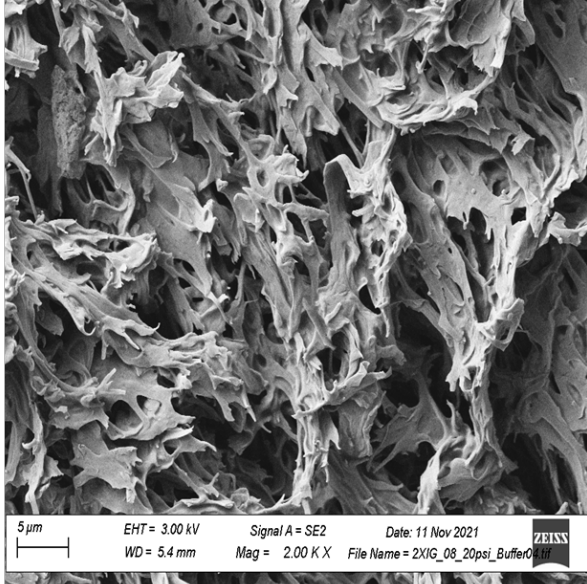
**Fouled 0.8 μm layer**
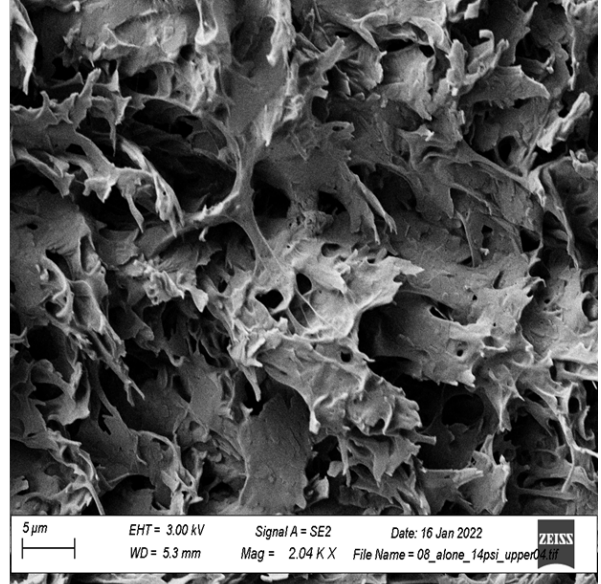
Clean 0.2 μm layer
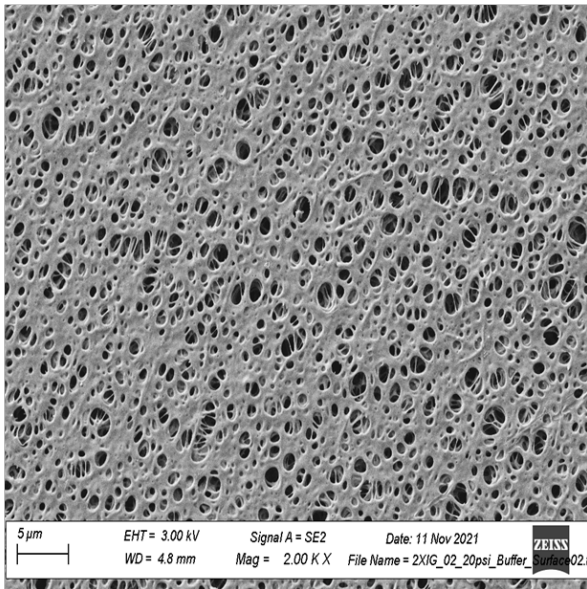
Fouled 0.2 μm layer

Figure 5: SEM images of the 0.8 and 0.2 μm layers of the Sartopore 2 XLG, after filtration of buffer (left) and after filtration of the LNPs (right) through the dual-layer filter at a pressure of 14 psi until a flux decline of more than 99%. Scale bars are 5 μm.

Pressure-Stepping Experiments

Although the results in Figures 1 to 5 provide important insights into the underlying filtration mechanisms, they do not explain the significant increase in capacity and reduction in the rate of fouling at higher TMP. The effects of pressure on the filtration behavior were examined more directly by performing pressure stepping experiments in which the TMP was varied in a step-wise fashion during a single filtration run, without any disruption in the LNP feed. The top panel of Figure 6 shows results in which the filtration was started at 14 psi for the first ≈150 s after which the pressure was abruptly decreased to 1 psi for 300 s before being returned to 14 psi. In both cases, the data are plotted as the resistance (evaluated directly from the flux and TMP data using Equation 1), as a function of filtration time. The initial step-down in pressure resulted in a 7-fold increase in resistance, while the final step-up in pressure resulted in a 6-fold reduction in resistance. This variation in resistance with TMP is at least qualitatively consistent with the higher capacity at higher TMP seen in Figure 1. The lower panel of Figure 6 shows results from a reverse pressure stepping experiment, starting the filtration at 1 psi and increasing the pressure to 14 psi before returning to 1 psi. In this case, the initial step-up in pressure caused a small (approximately 1.5-fold) increase in resistance, likely due to the relatively low level of fouling after the 150 s of filtration at low TMP, but the final reduction in TMP caused a 13-fold increase in resistance, similar to the behavior seen in the experiment that was started at 14 psi.

The observed dependence of resistance on pressure is surprising. An incompressible fouling deposit would give a resistance that is independent of pressure, while a compressible fouling deposit would show a resistance that is greater at high pressure (compression increases the packing density of the deposit, making it less permeable),[52] which is exactly the opposite of what is seen in Figure 6. The data obtained with the LNP suggest that traditional interpretations of compressible or incompressible fouling deposits are not applicable to this system; instead, the unique characteristics of the LNPs lead to a sharp reduction in resistance at high transmembrane pressures.
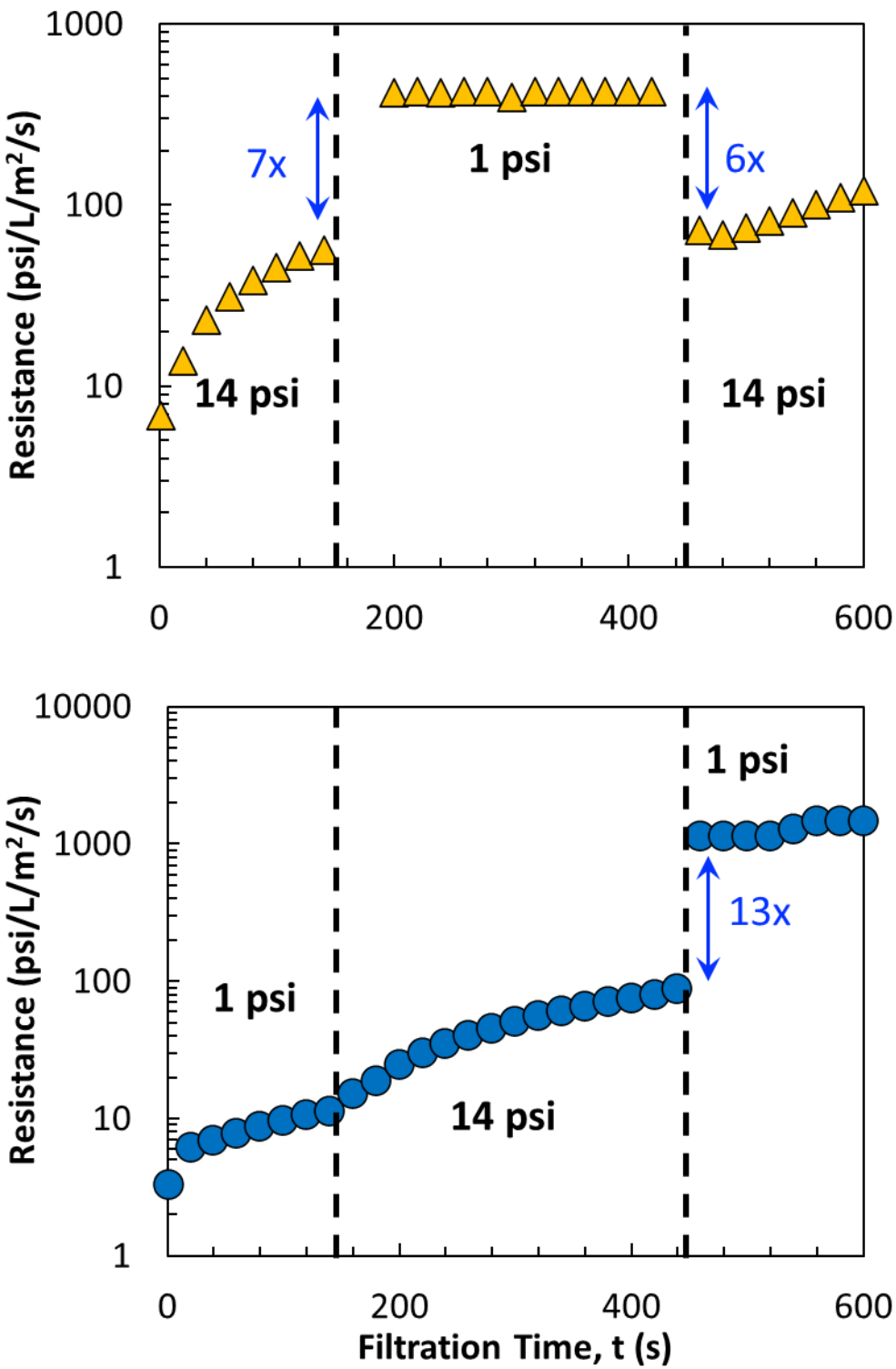
Figure 6: Resistance during pressure stepping experiments performed with the Sartopore 2 XLG membrane. Top panel: continuous filtration of the LNPs at 14 psi, 1 psi, and 14 psi. Bottom panel: continuous filtration of the LNPs at 1 psi,14 psi, and 1 psi.

The pressure stepping experiments demonstrate that the resistance of the fouled filter is a function of transmembrane pressure, although it is difficult to quantify the pressure dependence due to the continued fouling that occurs during the LNP filtration. The direct effect of pressure on the resistance was examined by first fouling the Sartopore 2 XLG with LNPs and then measuring the buffer flux through the fouled membrane at different TMP. To avoid de-pressurizing the system, the filter was fed by two pressure reservoirs, one containing the LNPs and one containing buffer, using a 3-way stopcock valve. The initial LNP filtration was conducted at a constant TMP of 14 psi until a flux decline of approximately 90%, with the feed then rapidly switched to buffer at the same TMP. The calculated values of the resistance during this experiment are summarized in Figure 7. The resistance of the fouled membrane while filtering buffer remained stable at a value approximately equal to that obtained at the end of the LNP filtration, indicating that the deposited foulants were quite stable (at least in response to a short buffer flush). The reduction in TMP from 14 to 1 psi caused a 3-fold increase in the resistance, corresponding to a 40-fold decrease in flux. The resistance returned to its previous value when the TMP was increased back to 14 psi, demonstrating that the behavior of the fouling deposit was fully reversible. Just as in Figure 6, the decrease in resistance with increasing TMP is completely opposite that expected for a compressible fouling deposit and is also different from the pressure-independent resistance expected for an incompressible fouling deposit. The pressure-dependent behavior is consistent across the multiple experiments shown in Figures 1, 6, and 7, suggesting that this phenomenon is intrinsic to the LNPs. One interpretation of the observed behavior is that increased pressure may deform the fouling deposit, e.g., at the entrance to a blocked pore, possibly due to a distortion of the LNPs when subjected to greater TMP. This behavior appears fully reversible, with the LNPs resuming their previous state when the TMP is reduced, restoring the high resistance of the fouling deposit.
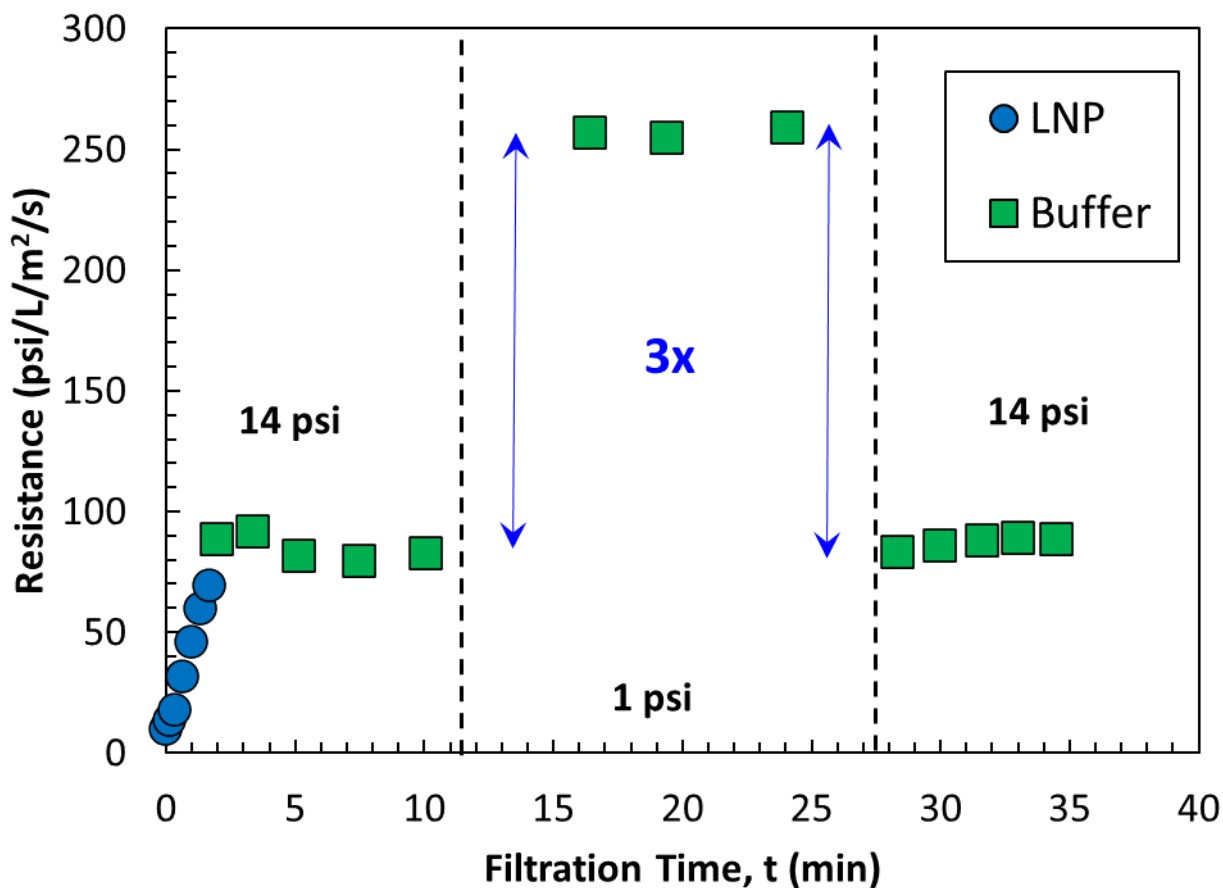
Figure 7: Total resistance during buffer permeability measurements performed with the Sartopore 2 XLG membrane. Filtration starts with LNPs at 14 psi followed by buffer at 14 psi, buffer at 1 psi, and then buffer at 14 psi.

Conclusions

The results presented in this study provide the first quantitative analysis of the sterile filtration behavior of mRNA-LNPs. Sterile filtration through a Sartopore 2 XLG dual-layer filter resulted in high (>96%) yields, and the filter capacity increased with increasing transmembrane pressure. The flux decline behavior was analyzed using a derivative plot, with the slope consistent with predictions of the complete pore blockage model. SEM images showed deposition of the LNPs on the surface of the 0.2 μm layer of the Sartopore 2 XLG. The 0.8 μm layer showed relatively little fouling, although it functioned as a prefilter that increased the capacity of the sterilizing-grade layer, presumably by removing a portion of the foulant species present in the feed.

The effect of pressure on the filtration of the LNPs was examined through a series of pressure stepping experiments in which the TMP was varied step-wise during a single continuous filtration. The resistance was found to decrease at high TMP, in contrast to the pressure-independent behavior expected for an incompressible foulant and opposite to the increase in resistance with increasing pressure expected for a compressible fouling deposit. This behavior suggests that operation at high TMP may cause a change in the structure of the LNP-fouled filter, leading to a decrease in fouling resistance. This behavior appears to be fully reversible based on data obtained during buffer flow measurements through the fouled filter. Future experiments will be required to further characterize the underlying factors governing the resistance of the fouled filter, including its dependence on the properties of both the LNPs and the membrane itself. The results obtained in this study provide important insights into the novel behavior observed during the sterile filtration of LNPs.

AUTHOR INFORMATION

Corresponding Author

Andrew L. Zydney – Department of Chemical Engineering, 404 Chemical & Biomedical Engineering Building, The Pennsylvania State University, University Park, PA, 16802, USA. E-mail address: zydney@engr.psu.edu

Authors

Kevork Oliver Messerian – Department of Chemical Engineering, 406 Chemical & Biomedical Engineering Building, The Pennsylvania State University, University Park, PA, 16802, USA. E-mail address: kdm5671@psu.edu

Anton Zverev – Technical Development, Moderna, Inc., Cambridge, MA 02162, USA, E-mail address: anton.zverev@modernatx.com

Jack F. Kramarczyk – Technical Development, Moderna, Inc., Cambridge, MA 02162, USA, E-mail address: jack.kramarczyk@modernatx.com

Author Contributions

Kevork Oliver Messerian – Data curation, formal analysis, investigation, and writing–original draft.
Anton Zverev – Methodology, resources, and writing–review and editing.

Jack Kramarczyk – Funding acquisition, Conceptualization, methodology, resources, and writing–review and editing.
Andrew L. Zydney – Conceptualization, Funding, Supervision, Writing – review & editing.

Notes

Acknowledgement

Figure Captions

Figure 2: Filtrate flux (upper panel) and resistance (lower panel) as a function of the volumetric throughput during constant pressure filtration of the LNP through the Sartopore 2 XLG capsules at pressures of 2, 8, 14 and 20 psi.

Figure 2: Derivative plot for LNP filtration at 2, 8, 14 and 20 psi through the Sartopore 2 XLG. The solid black and green lines represent a slope of 2 to guide the eye; these are not fits to the experimental data.

Figure 3: Filtrate flux as a function of the volumetric throughput for filtration through the individual layers of the Sartopore 2 XLG at TMP = 14 psi. Solid curves are model fits generated using the linearized form of the complete pore blockage model.

Figure 4: Filtrate flux as a function of volumetric throughput during filtration of the fresh LNP and previously filtered LNP through the Sartopore 2 XLG at 14 psi.

Figure 5: SEM images of the 0.8 and 0.2 µm layers of the Sartopore 2 XLG, after filtration of buffer (left) and after filtration of the LNPs (right) through the dual-layer filter at a pressure of 14 psi until a flux decline of more than 99%. Scale bars are 5 µm.

Figure 6: Resistance during pressure stepping experiments performed with the Sartopore 2 XLG membrane. Top panel: continuous filtration of the LNPs at 14 psi, 1 psi, and 14 psi. Bottom panel: continuous filtration of the LNPs at 1 psi,14 psi, and 1 psi.

Figure 7: Total resistance during buffer permeability measurements performed with the Sartopore 2 XLG membrane. Filtration starts with LNPs at 14 psi followed by buffer at 14 psi, buffer at 1 psi, and then buffer at 14 psi.

References

(1) Huang, Q., Zeng, J., & Yan, J. (2021). COVID-19 mRNA vaccines. *Journal of Genetics and Genomics*, *48*(2), 107–114. https://doi.org/10.1016/J.JGG.2021.02.006

(2) Nel, A. E., & Miller, J. F. (2021). Nano-Enabled COVID-19 Vaccines: Meeting the Challenges of Durable Antibody plus Cellular Immunity and Immune Escape. *ACS Nano*, *15*(4), 5793–5818. https://doi.org/10.1021/acsnano.1c01845

(3) Zieneldien, T., Kim, J., Cao, J., & Cao, C. (2021). Covid-19 vaccines: Current conditions and future prospects. *Biology*, *10*(10). https://doi.org/10.3390/biology10100960

(4) Anand, P., & Stahel, V. P. (2021). The safety of Covid-19 mRNA vaccines: a review. *Patient Safety in Surgery*, *15*(1), 22. https://doi.org/10.1186/s13037-021-00296-4

(5) Chung, Y. H., Beiss, V., Fiering, S. N., & Steinmetz, N. F. (2020). Covid-19 vaccine frontrunners and their nanotechnology design. *ACS Nano*, *14*(10), 12522–12537. https://doi.org/10.1021/acsnano.0c07197

(6) Xu, S., Yang, K., Li, R., & Zhang, L. (2020). mRNA Vaccine Era-Mechanisms, Drug Platform and Clinical Prospection. *International Journal of Molecular Sciences*, *21*(18). https://doi.org/10.3390/ijms21186582

(7) Pardi, N., Hogan, M. J., Porter, F. W., & Weissman, D. (2018). mRNA vaccines - a new era in vaccinology. *Nature Reviews. Drug Discovery*, *17*(4), 261–279. https://doi.org/10.1038/nrd.2017.243

(8) Reichmuth, A. M., Oberli, M. A., Jaklenec, A., Langer, R., & Blankschtein, D. (2016). mRNA vaccine delivery using lipid nanoparticles. *Therapeutic Delivery*, *7*(5), 319–334. https://doi.org/10.4155/tde-2016-0006.

(9) Park, K. S., Sun, X., Aikins, M. E., & Moon, J. J. (2021). Non-viral COVID-19 vaccine delivery systems. *Advanced Drug Delivery Reviews*, *169*, 137–151. https://doi.org/10.1016/j.addr.2020.12.008

(10) Zhou, X., Jiang, X., Qu, M., Aninwene, G. E. 2nd, Jucaud, V., Moon, J. J., Gu, Z., Sun, W., & Khademhosseini, A. (2020). Engineering Antiviral Vaccines. *ACS Nano*, *14*(10), 12370–12389. https://doi.org/10.1021/acsnano.0c06109

(11) Sahin, U., Karikó, K., & Türeci, Ö. (2014). mRNA-based therapeutics--developing a new class of drugs. *Nature Reviews. Drug Discovery*, *13*(10), 759–780. https://doi.org/10.1038/nrd4278

(12) Gómez-Aguado, I., Rodríguez-Castejón, J., Vicente-Pascual, M., Rodríguez-Gascón, A., Solinís, M. Á., & Del Pozo-Rodríguez, A. (2020). Nanomedicines to deliver mRNA: State

of the art and future perspectives. In *Nanomaterials* (Vol. 10, Issue 2). https://doi.org/10.3390/nano10020364

(13) Hajj, K. A., & Whitehead, K. A. (2017). Tools for translation: non-viral materials for therapeutic mRNA delivery. *Nature Reviews Materials*, *2*(10), 17056. https://doi.org/10.1038/natrevmats.2017.56

(14) Schoenmaker, L., Witzigmann, D., Kulkarni, J. A., Verbeke, R., Kersten, G., Jiskoot, W., & Crommelin, D. J. A. (2021). mRNA-lipid nanoparticle COVID-19 vaccines: Structure and stability. *International Journal of Pharmaceutics*, *601*, 120586. https://doi.org/10.1016/j.ijpharm.2021.120586

(15) Rietwyk, S., & Peer, D. (2017). Next-Generation Lipids in RNA Interference Therapeutics. *ACS Nano*, *11*(8), 7572–7586. https://doi.org/10.1021/acsnano.7b04734

(16) Brader, M. L., Williams, S. J., Banks, J. M., Hui, W. H., Zhou, Z. H., & Jin, L. (2021). Encapsulation state of messenger RNA inside lipid nanoparticles. *Biophysical Journal*, *120*(14), 2766–2770. https://doi.org/10.1016/j.bpj.2021.03.012

(17) Carvalho, S. B., Peixoto, C., Carrondo, M. T. J., & Silva, R. S. J. (2021). Downstream processing for influenza vaccines and candidates: An update. *BIOTECHNOLOGY AND BIOENGINEERING*, *118*(8), 2845–2869. https://doi.org/10.1002/bit.27803

(18) Tenchov, R., Bird, R., Curtze, A. E., & Zhou, Q. (2021). Lipid Nanoparticles-From Liposomes to mRNA Vaccine Delivery, a Landscape of Research Diversity and Advancement. *ACS Nano*. https://doi.org/10.1021/acsnano.1c04996

(19) Mitchell, M. J., Billingsley, M. M., Haley, R. M., Wechsler, M. E., Peppas, N. A., & Langer, R. (2021). Engineering precision nanoparticles for drug delivery. *Nature Reviews. Drug Discovery*, *20*(2), 101–124. https://doi.org/10.1038/s41573-020-0090-8

(20) Puri, A., Loomis, K., Smith, B., Lee, J.-H., Yavlovich, A., Heldman, E., & Blumenthal, R. (2009). Lipid-based nanoparticles as pharmaceutical drug carriers: from concepts to clinic. *Critical Reviews in Therapeutic Drug Carrier Systems*, *26*(6), 523–580. https://doi.org/10.1615/critrevtherdrugcarriersyst.v26.i6.10

(21) Torchilin, V. P. (2005). Recent advances with liposomes as pharmaceutical carriers. *Nature Reviews. Drug Discovery*, *4*(2), 145–160. https://doi.org/10.1038/nrd1632

(22) Gao, W., Hu, C.-M. J., Fang, R. H., & Zhang, L. (2013). Liposome-like Nanostructures for Drug Delivery. *Journal of Materials Chemistry. B*, *1*(48). https://doi.org/10.1039/C3TB21238F

(23) Buschmann, M. D., Carrasco, M. J., Alishetty, S., Paige, M., Alameh, M. G., & Weissman, D. (2021). Nanomaterial Delivery Systems for mRNA Vaccines. *Vaccines*, *9*(1). https://doi.org/10.3390/vaccines9010065

(24) Wahane, A., Waghmode, A., Kapphahn, A., Dhuri, K., Gupta, A., & Bahal, R. (2020). Role of Lipid-Based and Polymer-Based Non-Viral Vectors in Nucleic Acid Delivery for Next-Generation Gene Therapy. *Molecules (Basel, Switzerland)*, *25*(12). https://doi.org/10.3390/molecules25122866

(25) Chauhan, G., Madou, M. J., Kalra, S., Chopra, V., Ghosh, D., & Martinez-Chapa, S. O. (2020). Nanotechnology for COVID-19: Therapeutics and Vaccine Research. *ACS Nano*, *14*(7), 7760–7782. https://doi.org/10.1021/acsnano.0c04006

(26) Hou, X., Zaks, T., Langer, R., & Dong, Y. (2021). Lipid nanoparticles for mRNA delivery. *Nature Reviews. Materials*, *6*(12), 1078–1094. https://doi.org/10.1038/s41578-021-00358-0

(27) Rosa, S. S., Prazeres, D. M. F., Azevedo, A. M., & Marques, M. P. C. (2021). mRNA vaccines manufacturing: Challenges and bottlenecks. *Vaccine*, *39*(16), 2190–2200. https://doi.org/10.1016/j.vaccine.2021.03.038

(28) Whitley, J., Zwolinski, C., Denis, C., Maughan, M., Hayles, L., Clarke, D., Snare, M., Liao, H., Chiou, S., Marmura, T., Zoeller, H., Hudson, B., Peart, J., Johnson, M., Karlsson, A., Wang, Y., Nagle, C., Harris, C., Tonkin, D., … Johnson, M. R. (2022). Development of mRNA manufacturing for vaccines and therapeutics: mRNA platform requirements and development of a scalable production process to support early phase clinical trials. *Translational Research : The Journal of Laboratory and Clinical Medicine*, *242*, 38–55. https://doi.org/10.1016/j.trsl.2021.11.009

(29) Jackson, N. A. C., Kester, K. E., Casimiro, D., Gurunathan, S., & DeRosa, F. (2020). The promise of mRNA vaccines: a biotech and industrial perspective. *NPJ Vaccines*, *5*, 11. https://doi.org/10.1038/s41541-020-0159-8

(30) Zydney, A. L. (2021). New developments in membranes for bioprocessing – A review. *Journal of Membrane Science*, *620*, 118804. https://doi.org/10.1016/J.MEMSCI.2020.118804

(31) van Reis, R., & Zydney, A. (2007). Bioprocess membrane technology. *Journal of Membrane Science*, *297*(1–2), 16–50. https://doi.org/10.1016/J.MEMSCI.2007.02.045

(32) Moleirinho, M. G., Silva, R. J. S., Alves, P. M., Carrondo, M. J. T., & Peixoto, C. (2020). Current challenges in biotherapeutic particles manufacturing. *Expert Opinion on Biological Therapy*, *20*(5), 451–465. https://doi.org/10.1080/14712598.2020.1693541

(33) Zydney, A. L. (2009). Membrane Technology for Purification of Therapeutic Proteins. *BIOTECHNOLOGY AND BIOENGINEERING*, *103*(2), 227–230. https://doi.org/10.1002/bit.22308

(34) ASTM. Standard Test Method for Determining Bacterial Retention of Membrane Filters Utilized for Liquid Filtration. 2013;1–6.

(35) Jornitz, M., & Meltzer, T. H. (2008). Assuring sterility with ASTM F 838-83. *Pharmaceutical Technology Europe*, *20*, 41–45.

(36) Wright, E., Miller, J. J., Csordas, M., Gosselin, A. R., Carter, J. A., McGrath, J. L., Latulippe, D. R., & Roussie, J. A. (2020). Development of isoporous microslit silicon nitride membranes for sterile filtration applications. *BIOTECHNOLOGY AND BIOENGINEERING*, *117*(3), 879–885. https://doi.org/10.1002/bit.27240

(37) Taylor, N., Ma, W., Kristopeit, A., Wang, S. C., & Zydney, A. L. (2021). Evaluation of a sterile filtration process for viral vaccines using a model nanoparticle suspension. *Biotechnology and Bioengineering*, *118*(1), 106–115. https://doi.org/10.1002/bit.27554

(38) Emami, P., Fallahianbijan, F., Dinse, E., Motevalian, S. P., Conde, B. C., Reilly, K., & Zydney, A. L. (2021). Fouling Behavior during Sterile Filtration of Different Glycoconjugate Serotypes Used in Conjugate Vaccines. *Pharmaceutical Research*, *38*(1), 155–163. https://doi.org/10.1007/s11095-020-02983-w

(39) Zourna, K., Iwaniec, A., Turner, S., Jackson, N. B., & Welsh, J. H. (2021). Optimizing the Filtration of Liposomes Using Sterilizing-Grade Filters. *PDA Journal of Pharmaceutical Science and Technology*, *75*(2), 128–140. https://doi.org/10.5731/pdajpst.2020.011866

(40) Johnson, T. F., Jones, K., Iacoviello, F., Turner, S., Jackson, N. B., Zourna, K., Welsh, J. H., Shearing, P. R., Hoare, M., & Bracewell, D. G. (2021). Liposome Sterile Filtration Characterization via X-ray Computed Tomography and Confocal Microscopy. *Membranes*, *11*(11). https://doi.org/10.3390/membranes11110905

(41) Toh, M. R., & Chiu, G. N. C. (2013). Liposomes as sterile preparations and limitations of sterilisation techniques in liposomal manufacturing. *Asian Journal of Pharmaceutical Sciences*, *8*(2), 88–95. https://doi.org/10.1016/J.AJPS.2013.07.011

(42) Singh, B., Mundlamuri, R., Friese, T., Mundrigi, A., Handt, S., & Loewe, T. (2018). Benchmarking of Sterilizing-Grade Filter Membranes with Liposome Filtration. *PDA Journal of Pharmaceutical Science and Technology*, *72*(3), 223–235. https://doi.org/10.5731/pdajpst.2017.007757

(43) Folmsbee, M., & Moussourakis, M. (2012). Sterilizing filtration of liposome and related lipid-containing solutions: enhancing successful filter qualification. *PDA Journal of Pharmaceutical Science and Technology*, *66*(2), 161–167. https://doi.org/10.5731/pdajpst.2012.00771

(44) Hassett, K.J., Higgins, J., Woods, A., Levy, B., Xia, Y., Hsiao, C.J., Acosta, E., Almarsson, O., Moore, M.J., Brito, L.A. (2021). Impact of lipid nanoparticle size on mRNA vaccine immunogenicity. *Journal of Controlled Release*, 335, 237-246.

(45) Jornitz, M.W. *Sterile filtration*. 1st ed; Springer: Berlin, 2006; pp 46-48.

(46) Hermans PH, Bredee HL. Principles of the mathematical treatment of constant-pressure filtration. *Journal of the Society of the Chemical Industry* 55T: 1-4 (1936).

(47) Peles, J., Fallahianbijan, F., Cacace, B., Carbrello, C., Giglia, S., & Zydney, A. L. (2022). Effect of operating pressure on protein fouling during constant-pressure virus removal filtration. *Journal of Membrane Science*, *648*, 120351. https://doi.org/10.1016/J.MEMSCI.2022.120351

(48) Iritani, E., Katagiri, N., Takenaka, T., & Yamashita, Y. (2015). Membrane pore blocking during cake formation in constant pressure and constant flux dead-end microfiltration of very dilute colloids. *Chemical Engineering Science*, *122*, 465–473. https://doi.org/10.1016/J.CES.2014.09.052

(49) Ho, C. C., & Zydney, A. L. (2000). A Combined Pore Blockage and Cake Filtration Model for Protein Fouling during Microfiltration. *Journal of Colloid and Interface Science*, *232*(2), 389–399. https://doi.org/10.1006/jcis.2000.7231

(50) Xu, H., Xiao, K., Yu, J., Huang, B., Wang, X., Liang, S., Wei, C., Wen, X., & Huang, X. (2020). A Simple Method to Identify the Dominant Fouling Mechanisms during Membrane Filtration Based on Piecewise Multiple Linear Regression. *Membranes*, *10*(8). https://doi.org/10.3390/membranes10080171

(51) Iritani, E., & Katagiri, N. (2016). Developments of Blocking Filtration Model in Membrane Filtration. *KONA Powder and Particle Journal*, *33*, 179–202. https://doi.org/10.14356/kona.2016024

(52) Mendret, J., Guigui, C., Schmitz, P., & Cabassud, C. (2009). In situ dynamic characterisation of fouling under different pressure conditions during dead-end filtration: Compressibility properties of particle cakes. *Journal of Membrane Science*, *333*(1–2), 20–29. https://doi.org/10.1016/J.MEMSCI.2009.01.035